Journal of Power Sources 656 (2025) 238083

Contents lists available at ScienceDirect

Journal of Power Sources

journal homepage: www.elsevier.com/locate/jpowsour

# Conversion of methane into value-added products in catalytic-assisted solid oxide fuel cell

Vanessa B. Vilela [a,b], Franck Fournet-Fayard [b], Marlu C. Steil [b], Vivian V. Thyssen [a], Daniel Z. de Florio [c], Andre S. Ferlauto [c], Fabio C. Fonseca [a,*]

[a] Nuclear and Energy Research Institute, IPEN-CNEN, 05508-000, São Paulo, SP, Brazil
[b] Univ. Grenoble Alpes, Univ. Savoie Mont Blanc, CNRS, Grenoble INP, LEPMI, 38000, Grenoble, France
[c] Centre for Engineering, Modelling and Applied Social Sciences, Federal University of ABC, UFABC, 09210-580, Santo André, SP, Brazil

## HIGHLIGHTS

- $La_{0.5}Ce_{0.5}O_{2-\delta}$ catalyst is active for $O_2$-OCM and $H_2O$-OCM reactions.
- SOFC with LCO catalytic layer co-generates $C_2$ hydrocarbons, syngas, and electricity.
- $C_2$ selectivity shows a strong dependence on SOFC operating parameters.
- LCO catalytic layer promotes methane conversion and prevents carbon deposition.

## GRAPHICAL ABSTRACT

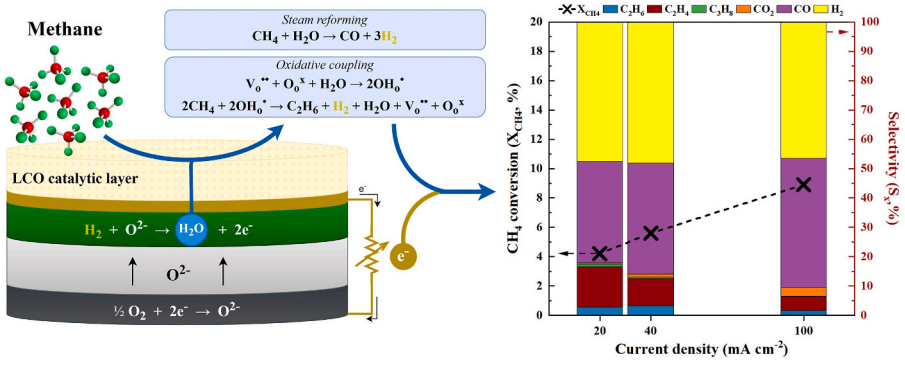


## ARTICLE INFO

*Keywords:*
Methane conversion
Solid oxide fuel cell
Catalytic layer
OCM
Syngas
Cogeneration

## ABSTRACT

Separating catalytic and electrochemical reactions at the fuel electrode of the direct methane solid oxide fuel cell (SOFC) produces syngas and $C_2$ products (ethane and ethylene), while cogenerating electricity. A SOFC-compatible $La_{0.5}Ce_{0.5}O_{2-\delta}$ catalyst is first validated for the oxidative coupling of methane (OCM) reactions with $O_2$ and $H_2O$ oxidizing agents in a fixed-bed reactor. It is then applied as a catalytic layer on the current collector of a standard nickel/yttria-stabilized zirconia (Ni/YSZ) anode. A systematic study of operating parameters such as temperature, fuel concentration, flow rate, and applied current reveals a maximum $C_2$ production rate of 1.5 mmol $min^{-1}$ $cm^{-2}$ and over 50 % selectivity for syngas ($H_2/CO \sim 1$). Experimental results, supported by thermodynamic data, indicate that steam generated by electrochemical hydrogen oxidation promotes both steam reforming and methane oxidative coupling within the catalytic layer, ensuring stable SOFC operation. This innovative fuel electrode configuration, featuring an OCM-active layer, enables efficient catalytic-assisted conversion of methane into value-added products within a SOFC.

* Corresponding author.
*E-mail address:* fabiocf@usp.br (F.C. Fonseca).

https://doi.org/10.1016/j.jpowsour.2025.238083
Received 15 May 2025; Received in revised form 5 August 2025; Accepted 7 August 2025
Available online 13 August 2025

## 1. Introduction

The search for alternative routes to produce chemical products using carbon sources other than fossil ones is gaining momentum due to growing demand for petrochemicals and the urgent need for more sustainable chemicals and fuels [1]. One effective strategy involves using natural gas as a feedstock to produce chemical compounds instead of burning it as a regular $CO_2$-emitting fuel with potentially harmful greenhouse effects by spills of methane ($CH_4$). This approach leverages the existing infrastructure and wide availability of natural gas to efficient processes to convert $CH_4$ into high-value-added chemical products. Notable products derived from methane include oxygenates such as methanol ($CH_3OH$), hydrocarbons such as ethane ($C_2H_6$) and ethylene ($C_2H_4$), and hydrogen (syngas) [2]. It is worth mentioning that the increasing relevance of biogas as a sustainable source of biomethane can also boost the production of such chemicals from renewable sources.

Traditionally, methane is converted into valuable chemicals through multistep processes. The first step involves steam reforming of methane (SRM) to produce syngas ($CO + H_2$), according to Reaction 1. Alongside SRM, the water-gas shift (WGS) reaction, in which water and carbon monoxide react to generate additional hydrogen and carbon dioxide, is usually associated (Reaction 2).

$$CH_4 + H_2O \rightarrow CO + 3H_2 \ \Delta H^{o}_{25^{\circ}C} = 206 \text{ kJ mol}^{-1} \quad \text{(R1)}$$

$$CO + H_2O \leftrightarrow CO_2 + H_2 \ \Delta H^{o}_{25^{\circ}C} = -41.1 \text{ kJ mol}^{-1} \quad \text{(R2)}$$

Subsequently, the Fischer-Tropsch process is employed to generate alkenes, or catalytic conversion processes are used to produce methanol. A more economically viable and environmentally friendly alternative is the direct conversion of methane to products. $C_2$ hydrocarbons, including $C_2H_6$ and $C_2H_4$, can be directly produced by the oxidative coupling of methane (OCM), as described by the global Reactions 3 and 4 [3,4]. Such reaction faces significant intrinsic challenges because of the high stability of methane conferred by the C-H bond strength (439.3 kJ $mol^{-1}$), low electron affinity, high ionization energy, and limited polarizability [5,6]. Despite extensive research efforts, the conventional OCM often suffers from excessive methane oxidation, which leads to non-ideal $C_2$ yields for the commercialization of this technology [7].

$$2CH_4 + \tfrac{1}{2}O_2 \rightarrow C_2H_6 + H_2O \ \Delta H^{o}_{25^{\circ}C} = -177 \text{ kJ mol}^{-1} \quad \text{(R3)}$$

$$2CH_4 + O_2 \rightarrow C_2H_4 + 2H_2O \ \Delta H^{o}_{25^{\circ}C} = -282 \text{ kJ mol}^{-1} \quad \text{(R4)}$$

A relatively less explored approach for converting methane to products is through electrochemical processes based on the synergistic control of electrochemical oxidation/reduction reactions. This concept is based on using an oxide ion conducting electrolyte in a solid oxide cell (SOC), as depicted in Reactions 5 and 6. Note that the water produced electrochemically in situ (R5) reacts with methane to produce syngas, according to R1. When powered by renewable energy and feedstocks, SOC-based processes offer the potential for low or even carbon-neutral emissions, presenting a promising pathway for sustainable chemical and fuel production. The main challenge lies in the development of electrocatalysts and electrochemical reactor designs that simultaneously delivering high energy efficiency, long-term stability, and sufficient product yield to ensure economic feasibility [8–10].

$$CH_4 + 3O^{2-} \leftrightarrows CO + 2H_2O + 6e^- \quad \text{(R5)}$$

$$2CH_4 + 2O^{2-} \leftrightarrows C_2H_4 + 2H_2O + 4e^- \quad \text{(R6)}$$

Industrial electrochemical technologies, such as fuel cells and electrolyzers, are the main technological background to advance the electrochemical synthesis of petrochemicals to commercial scales [10]. Operating at 600–1000 °C, SOCs meet the thermal requirements for the direct catalytic conversion of methane into $C_2$ hydrocarbons. In these systems, oxide ions generated at the cathode migrate through the electrolyte and react with methane at the fuel electrode. A major advantage is the ability to control oxygen supply by adjusting the current in either fuel cell (SOFC) or electrolysis mode (SOEC) [11,12].

Several studies have highlighted interesting aspects of $CH_4$ conversion in SOC-type electrochemical reactors, emphasizing the co-generation of electricity and chemicals [13,14]. These studies suggested that combining electrochemical and catalytic reactions in the fuel electrode of SOFC is a promising strategy for methane conversion.

When standard Ni-based SOFC anodes are exposed to carbon-containing fuels, complete dehydrogenation often leads to coke formation on the anode surface and cell deactivation [15–17]. To mitigate this, alternative anode materials that combine catalytic activity for OCM reaction with the electrochemical properties required for SOFC operation have been explored, such as Li-doped NiO [18] and LSGM [19], $La_xSr_{0.9-x}TiO_{3-\delta}$ [20], $Sr_2Fe_{1.5}Mo_{0.5}O_{6-\delta}$ [9], $BaMg_{0.33}Nb_{0.67-x}Fe_{3x}O_{3-\delta}$ [21], $Na_2WO_4$-based [22,23], and $La_2O_3$-based [24,25]. These oxides help suppress total methane oxidation, but their low electronic conductivity limits SOFC performance and $C_2$ product yield when used directly as anode materials. Therefore, the development of advanced anode materials with high catalytic activity, mixed ionic–electronic conductivity, thermal and mechanical stability, coke resistance, and SOFC compatibility remains a key challenge for realizing efficient methane electrochemical conversion.

In this context, a strategy emerges to maintain the state-of-the-art Ni/YSZ anode composite combined with an additional catalytic layer tailored for the target reaction. This approach involves separating the catalytic and electrochemical functions of the fuel electrode. This can be achieved by adding a catalytic layer on top of the Ni/YSZ anode, as illustrated in Fig. 1. The added layer is electrically disconnected from the SOFC circuit and processes carbon-containing fuels by thermocatalytic reactions. Moreover, it can act as a protective barrier for the underlying anode layers from direct fuel exposure and thereby preventing carbon deposition. This anode architecture was initially designed for the partial oxidation of propane [26] and for internal steam reforming reactions, utilizing the water produced by the anodic electrochemical reactions. The water generated is used in the porous catalytic layer to promote fuel conversion through catalytic reforming. This anode architecture proved to be efficient for both direct methane and ethanol-fueled SOFCs [27–30]. Similarly, the water produced by hydrogen oxidation is the main oxidant for the OCM reaction in the catalytic layer (Fig. 1). A rather limited number of studies have investigated $H_2O$ as an oxidant for OCM ($H_2O$-OCM) to minimize the non-selective oxidation of $CH_4$ in fixed-bed reactors [31,32]. Such studies demonstrated that a high $H_2O$ partial pressure promoted $C_2$ formation. A $CH_4$-fueled SOFC can take advantage of the electrochemically produced $H_2O$ to enhance $C_2$ hydrocarbon formation when combined with a suitable catalytic layer. Such multiple reactions make a direct prediction of the system stability and products a complex task.

Developing a coke-resistant catalyst for OCM is a significant challenge for methane conversion in SOFC [15–17]. Carbon deposition typically results from side reactions such as methane cracking and the Boudouard reaction, as described in Reactions 7 and 8, respectively.

$$CH_4 \rightarrow C_{(s)} + 2H_2 \ \Delta H^{o}_{25^{\circ}C} = 75 \text{ kJ mol}^{-1} \quad \text{(R7)}$$

$$2CO \rightarrow CO_2 + C_{(s)} \ \Delta H^{o}_{25^{\circ}C} = 172.5 \text{ kJ mol}^{-1} \quad \text{(R8)}$$

A catalytic active layer tailored for methane coupling that is coke-resistant and compatible with SOFC components can achieve a stable reaction pathway for producing high value-added chemicals. Cerium oxide ($CeO_2$), known for its high oxygen storage capacity via the $Ce^{4+}/Ce^{3+}$ redox pair, is active for partial oxidation of methane, but lacks selectivity for OCM due to its limited ability to form electrophilic oxygen species [33,34]. To improve $C_2$ selectivity, $CeO_2$ has been combined with rare earth metal oxides. The $La_{0.5}Ce_{0.5}O_{2-\delta}$ (LCO) is emphasized for its high basicity and ability to generate active electrophilic oxygen species, making it a chemically stable and active catalyst when $La^{3+}$ is incorporated into the $CeO_2$ lattice [35,36]. Furthermore, LCO has been

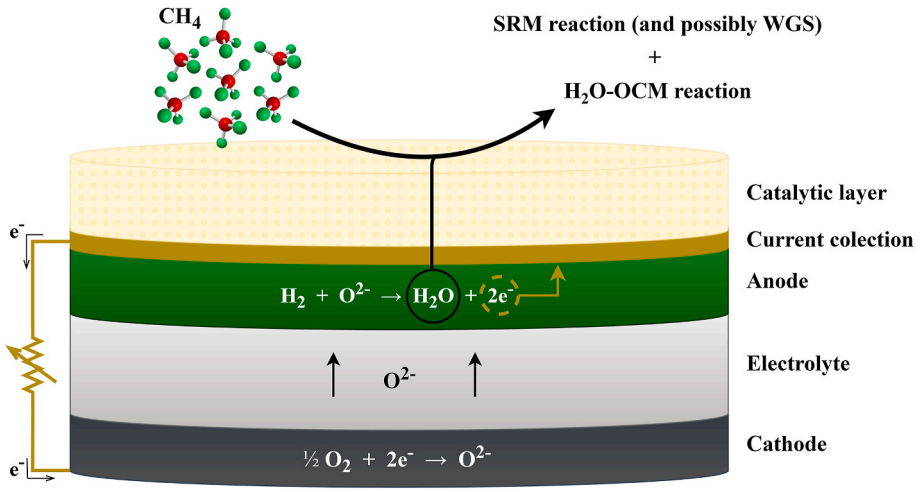


**Fig. 1.** Schematics of the device configuration and main reactions for methane conversion in the SOFC with catalytic and anode layers in the fuel electrode.

evaluated as both an electrolyte and electrode material in oxide-ion and proton-conducting SOCs, confirming its compatibility with this technology [37].

The objective of this study is to investigate a fuel electrode design for SOFC, as depicted in Fig. 1, aimed at producing value-added chemicals using an OCM active $La_{0.5}Ce_{0.5}O_{2-\delta}$ (LCO) catalytic layer. The catalytic properties of LCO were investigated towards $H_2O$-OCM, and electrolyte-supported SOFCs, with an integrated LCO layer, were fabricated and operated on direct methane under various conditions. The goal was to optimize methane conversion and $C_2$ product selectivity while maintaining stable SOFC operation.

## 2. Experimental

### 2.1. Catalyst preparation and characterization

$La_{0.5}Ce_{0.5}O_{2-\delta}$ catalyst was prepared by the combustion method with 150 % excess of urea [38]. Lanthanum nitrate ($LaNO_3)_3.6H_2O$, 99.9 %, Sigma-Aldrich), cerium nitrate ($Ce(NO_3)_3.6H_2O$, 99.9 %, Sigma-Aldrich), and urea ($CH_4N_2O$, Nuclear) were dissolved in 10 mL of deionized water, achieving a solution with urea/nitrate ratio of 6.25. The mixed solution was maintained under magnetic stirring and constant heating at 80 °C until a viscous gel was formed. The obtained gel was placed in a preheated muffle furnace at 500 °C to initiate the combustion reaction. After the reaction, the muffle furnace was cooled to 25 °C, and the resulting material was homogenized using a mortar and pestle, thus obtaining the final powder.

X-ray diffraction (XRD) analysis of the synthesized catalyst was carried out in a Rigaku MiniFlex II with $CuK_\alpha$ radiation source (0.15406 nm) in the range of 20 to 80° 2θ degree, and the crystalline phases were identified by Crystallograhica Search Match© software. The lattice parameters were determined by treating the diffractograms using the Rietveld refinement method with TOPAS® Academic 7 software (Bruker AXS). Semi-quantitative compositional analysis of the samples was conducted using wavelength dispersive X-ray fluorescence (WDXRF) in a Rigaku Supermini200. The microstructure of the as-prepared powder was analyzed by a Zeiss Ultra 55 FEG scanning electron microscope (SEM) with acceleration voltage of 20 kV and different magnitudes (x 5k, 20k, and 50k). The average grain diameter was estimated using ImageJ software. Raman spectra of as-prepared and spent (after catalytic tests) LCO powders were acquired using a Renishaw InVia Raman Spectrometer in micro-Raman configuration (objective x50) with a green line provided by an Ar-ion laser (514 nm).

The catalytic activity of LCO for the OCM reaction was evaluated in a fixed-bed quartz flow reactor at atmospheric pressure. Both oxygen ($O_2$-OCM) and water ($H_2O$-OCM) were used as oxidants. 50 mg of catalyst was placed in the middle of the quartz tube with quartz wool and pretreated in nitrogen gas at 850 °C for 30 min. Following the treatment, the reactant mixture ($CH_4$ and oxidant), balanced in nitrogen, was introduced at a total flow rate of 60 mL $min^{-1}$. For $O_2$-OCM test, the $CH_4$:$O_2$ molar ratio was 4:1, while for $H_2O$-OCM, $CH_4$:$H_2O$ was 2:1. Steam was introduced into the reactor by flowing nitrogen through water saturator. All reactions were carried out at 850 °C. The reactor effluent was quantitatively analyzed by an online GC/MS system (GC 7890B, Agilent), equipped with two columns (Plot-U and molecular sieve), each coupled to a thermal conductivity detector (TCD) and a flame ionization detector (FID). Methane conversion ($X_{CH4}$) and product selectivity ($S_x$) were calculated from the outlet gas composition according to Equations (1) and (2).

$$X_{CH_4}\,(\%) = \frac{\dot{n}^{in}_{CH_4} - \dot{n}^{out}_{CH_4}}{\dot{n}^{in}_{CH_4}} \cdot 100 \qquad \text{(Eq. 1)}$$

$$S_x\,(\%) = \frac{(c_x \cdot \dot{n}_x)}{\sum_{products}(c_i \cdot \dot{n}_i)} \cdot 100 \qquad \text{(Eq. 2)}$$

where $\dot{n}^{in}_{CH_4}$ and $\dot{n}^{out}_{CH_4}$ are the inlet and outlet molar flow rates of methane, respectively; $\dot{n}_x$ is the molar flow rate and $c_x$ is the number of carbon atoms in product $x$ (with $x$ = $C_2H_4$, $C_2H_6$, $C_3$, CO, $CO_2$, and $H_2$); and $\sum_{products}(c_i \cdot \dot{n}_i)$ represents the total molar flow rate of all detected gas-phase products. Note that possible carbon deposits and produced water were not included in the analysis.

### 2.2. Preparation of fuel cell with catalytic layer

Electrolyte-supported single cells were fabricated using a YSZ-8 (Tosoh) substrate (diameter ~ 19 mm, thickness ~ 0.45 mm), which was obtained through uniaxial pressing (1 ton $cm^{-2}$) of the powder, followed by isostatic pressing (2500 bar) and sintering at 1450 °C for 2 h. Electrolyte thickness was adjusted to 450 μm by diamond grinding. As cathode materials, LSM ($La_{0.65}Sr_{0.30}MnO_{3-\delta}$, Praxair) and 50 % LSM-50 % YSZ were used as cathode current collector (CCL) and functional (CFL) layers, respectively. The anode consisted of a 40 % NiO-60 % YSZ anode functional layer (AFL) and a 60 % NiO-40 % YSZ anode current collector (ACL) layer. Fig. S1a shows the fabricated electrolyte-supported single-cell with a catalytic layer schematic diagram.

Electrode inks were prepared using KD2921 (Zschimmer & Schwarz) as the organic vehicle, and Sigmacell type-50 cellulose ($(C_6H_{10}O_5)_n$, Sigma-Aldrich) was used as the pore-former. The functional layers contained 10 % pore former, while the collector layers contained 20 %, relative to the mass of the active material. All slurries were homogenized

using a planetary ball mill (MicroMill Pulverisette 7, Fritsch) and deposited by screen printing (C890, Aurel). The anode and cathode were sintered in air at 1400 °C and 1100 °C, respectively, for 1 h. Both electrodes had an active area of 1.2 $cm^2$. A gold wire was attached to the top of the CA layer with gold paste and annealed at 900 °C in air for 1 h. The catalytic layer ink was prepared by planetary ball milling a mixture composed of 30 wt% solids (80 wt% LCO + 20 wt% cellulose, SigmaCell type-50), 35 wt% ethanol (EtOH, Fischer Scientific), 31.5 % terpineol ($C_{10}H_8O$, Fischer Scientific), 2.3 wt% polyvinyl butyral ($(C_8H_{14}O_2)_n$, 36000 g $mol^{-1}$, Sigma-Aldrich), and 1.2 wt% polyvinylpyrrolidone ($(C_6H_9NO_2)_n$, 40000 g $mol^{-1}$, Fischer Scientific). The LCO catalytic layer was deposited onto the CA layer and gold wire using an air spray valve (SV 600) with a controller (VM60, Eleco EFD) mounted on a tabletop robot (TTA, IAI Corp). The target thickness was based on previously reported studies by the group [28,39,40]. Sintering of the catalytic layer was carried out at 900 °C for 1 h in air. Images of the anode surface, showing the Au current collector and the LCO catalytic layer, are provided in Fig. S1b. SEM images were collected to analyze the microstructure of the deposited catalytic layer. The average porosity and particle size were estimated using ImageJ software.

### 2.3. Electrochemical characterization and methane conversion tests

For the electrochemical experiments, the single cell was assembled in a 2-atm test bench comprising two alumina tubes (serving as anodic and cathodic chambers) separated by an alumina sample holder. A gold ring was used to seal the sample holder to the anode chamber, while the SOFC was fixed and sealed using a glass paste consisting of 70 % glass powder (Glass 8422, Schott) and 30 % terpineol ($C_{10}H_8O$, Fischer Scientific). The experimental setup is illustrated in Fig. S1c.

Prior to operation, the anode was reduced at 800 °C in a hydrogen atmosphere (10 % $H_2$/He, 50 mL $min^{-1}$) for 2 h. Throughout all tests, synthetic air (90 mL $min^{-1}$) was continuously supplied to the cathodic chamber. Electrochemical characterization under $H_2$ was conducted at 750, 800, and 850 °C measuring current-voltage-power (i-V-P) curves. All electrochemical measurements were performed using a Solartron 1280B potentiostat. During open-circuit voltage (OCV) operation, the SOFC was run on hydrogen (10 % $H_2$/He) to protect the Ni/YSZ anode from carbon deposition while stabilizing measurement conditions for methane conversion. At the start of each methane conversion test, after the fuel cell was polarized, the fuel feed was promptly switched from hydrogen to methane (balanced in He), ensuring that all subsequent catalytic performance evaluations were conducted with methane as the sole fuel.

Methane conversion in catalytic-assisted SOFC with different $CH_4$ concentrations (10 %, 50 %, and 100 %) were carried out to determine the optimal fuel composition. Catalytic performance under methane was further investigated under key operating parameters: temperature (750, 800, and 850 °C), anode inlet flow rate (10, 25, and 50 mL $min^{-1}$), and generated current (20, 40, and 100 mA $cm^{-2}$). For each experimental condition, the electrochemical parameters were recorded for ~2 h. The anode outlet was continuously analyzed by an online gas analysis system composed of a mass spectrometer (OmniStar ThermoStar, Pfeiffer Vacuum) and a micro gas chromatograph (R3000 MicroGC, SRA Instruments) equipped with four columns (PoraPlot U, PoraPlot Q, and two Molsieve-5A) and a TCD detector. Water vapor was removed from the product stream using a condensation system before entering the gas analysis system. The measured gas compositions were determined after the system reached stable conditions, at a fixed fuel cell voltage to stabilize the system and ensure adequate purging of the anode chamber and gas lines. Catalytic performance was calculated using the same methodology applied to the fixed-bed reactor tests (Eqs. (1) and (2)). It is important to note that the conversion and selectivity calculations did not consider possible carbon deposition or the formation of water among the products.

After the $CH_4$ conversion experiments, the SOFC was characterized by SEM and Raman spectroscopy to assess eventual structural and compositional changes. Raman spectra were first collected in various regions of the LCO layer surface. Subsequently, the catalytic layer was removed and Raman analysis was carried out directly at Ni/YSZ collector anode surface allowing a detailed investigation of the fuel electrode.

## 3. Results and discussion

### 3.1. Synthesis, characterization, and catalytic performance of powdered catalysts

Fig. 2a shows the XRD data for the as-prepared $La_{0.5}Ce_{0.5}O_{2-\delta}$ powder (ICSD 188491), which corresponds to a single-phase solid solution with a fluorite-type structure similar to $CeO_2$ (ICSD 24887) was observed. Compared to ceria, the main diffraction peak (111) shifts to a lower Bragg angle from 2θ ~28.40°–27.55° when La is added. This shift indicates lattice expansion due to the substitution of $Ce^{4+}$ (0.97 Å) with the larger $La^{3+}$ ions (1.16 Å), confirming the successful formation of LCO solid solution. Rietveld refinement (Table S1) further confirmed its defective disordered cubic fluorite structure (*Fm-3m*) with a lattice parameter of 5.5925(2) Å [41,42].

The crystal structure of La-doped $CeO_2$ is a debated topic, with both fluorite- or pyrochlore-type structures have been proposed for $La_{0.5}Ce_{0.5}O_{2-\delta}/La_2Ce_2O_7$ [43]. However, the absence of superstructure peaks associated with the pyrochlore phase in the 2θ range of ~30°–45° suggests that no pyrochlore-type ordering is present under the synthesis conditions used (Fig. 2a). The stabilization of $A_2B_2O_7$ pyrochlore structure is favored when the tolerance factor is ≥ 1.4, and as the difference between $r_{A^{3+}}$ and $r_{B^{4+}}$ decreases, a transition to smaller disordered fluorite-type unit cell occurs. In the case of LCO, the tolerance factor is 1.33, based on $La^{3+}$ (1.16 Å) and $Ce^{4+}$ (0.97 Å), both in 8-fold coordination [42,44]. As no additional heat treatment was carried out after the combustion synthesis, the formation of a pyrochlore-type structure is not expected.

Structural and surface defects play a crucial role in enhancing catalytic activity in OCM reactions. The defect chemistry and local disorder in LCO were investigated by Raman spectroscopy (Fig. 2b). The Raman spectrum of LCO displays five characteristic bands. The $F_{2g}$ band at 445 $cm^{-1}$ corresponds to Ce−$O_8$ lattice vibrations, typical of the fluorite structure (as observed in the $CeO_2$ spectrum). At ~255 $cm^{-1}$, a band attributed to the transverse optical (TO) modes is observed due to the anionic sublattice's disordering. The V-O band positioned in 570 $cm^{-1}$ is associated with oxygen vacancies resulting from the random distribution of $La^{3+}$ and $Ce^{4+}$ ions, which generate compensating defects to maintain charge neutrality. These vacancies facilitate the dissociative adsorption of $O_2$ molecules, promoting the formation of reactive oxygen species such as $O_2^{2-}$, $O_2^-$, and $O^-$. Bands at ~1100 $cm^{-1}$ and 1198 $cm^{-1}$ are assigned to surface carbonate species formed via reaction with atmospheric $CO_2$, and to superficial electrophilic $O_2^-$ species. These features confirm the formation of accessible oxygen sites across the surfaces of the catalyst. The formation of surface oxygen species will likely promote active sites for the OCM reaction contributing to a more selective catalyst [44,45].

SEM images of LCO (Fig. 2c), increasing magnification from left to right, reveal a porous microstructure composed of agglomerated particles (in the μm range size) with irregular shapes, characteristic of sponge-like structures formed by combustion synthesis. A higher magnification image (right panel in Fig. 2c) reveals distinguishable grains with calculated average size 90 nm. EDX mapping (Fig. 2d) confirms a homogeneous distribution of La and Ce throughout the scanned area, in agreement with the nominal composition determined by WDXRF (Table S2). These results, together with the XRD analysis, confirm that La and Ce cations are uniformly incorporated into the crystalline structure of $La_{0.5}Ce_{0.5}O_{2-\delta}$ solid solution.

To effectively use $La_{0.5}Ce_{0.5}O_{2-\delta}$ as a catalytic layer for methane

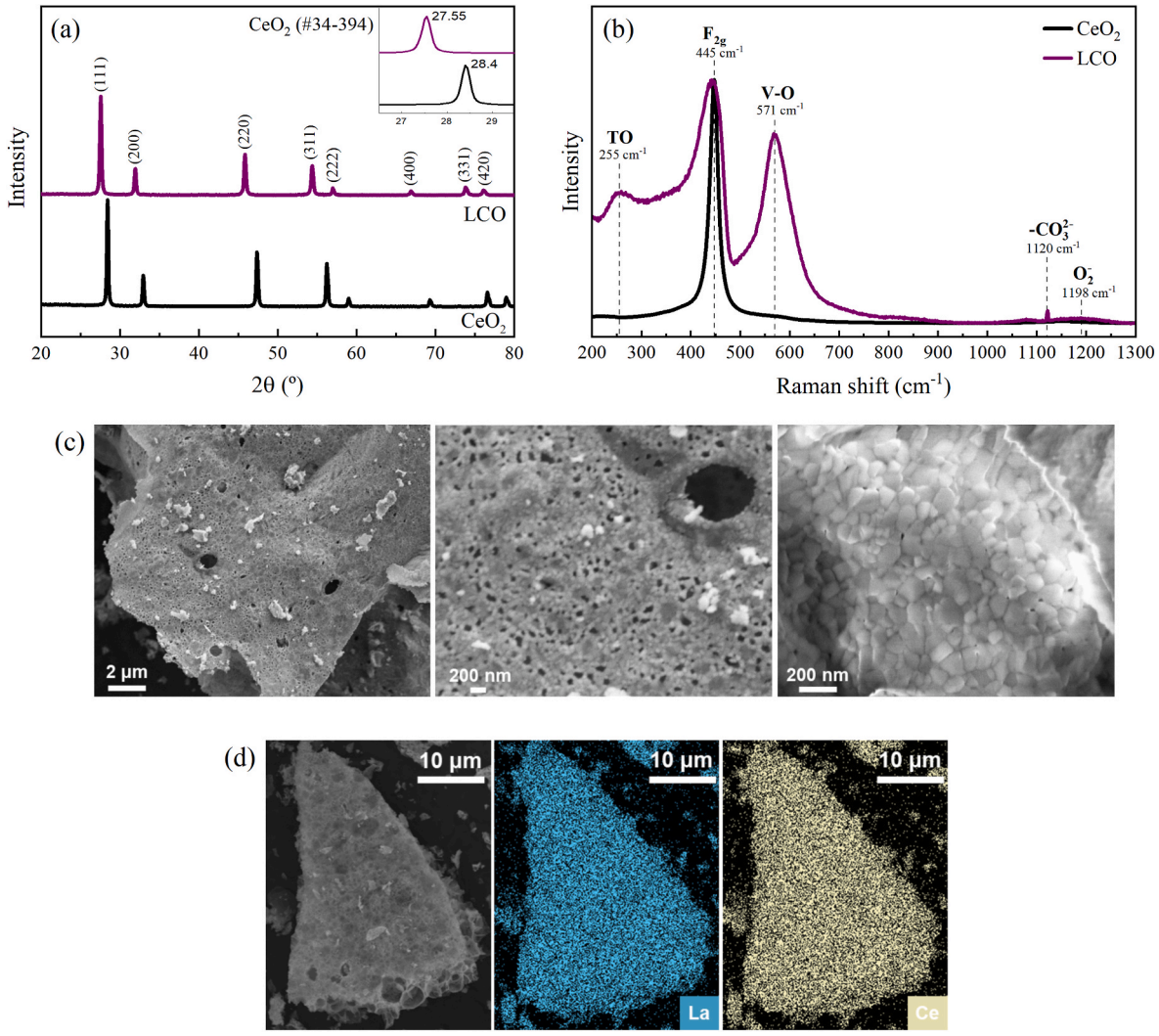


**Fig. 2.** (a) XRD pattern showing the crystalline structure, (b) Raman spectra illustrating the vibrational modes, (c) SEM images with increasing magnification (x 5k, 20k, and 50k from left to right), and (d) SEM image and the corresponding EDX elemental mapping of La and Ce for $La_{0.5}Ce_{0.5}O_{2-\delta}$ powder.

conversion in the SOFC, its catalytic properties were first investigated in a fixed bed reactor. The methane conversion and product selectivity for OCM reactions with both $O_2$ and $H_2O$ oxidants are shown in Fig. 3.

The OCM reaction is characterized by three main steps: (i) adsorption of gaseous oxygen on the catalyst surface; (ii) methyl radicals are formed by C-H cleavage of $CH_4$ molecule by its interaction with superficial oxygen species; and (iii) coupling of the methyl radicals to produce $C_2$ hydrocarbons in a gas phase pathway. Following the creation of methyl radicals, $C_2H_6$ is generated and subsequently undergoes dehydrogenation through either the surface or gas phase, resulting in $C_2H_4$ formation. The ethylene to ethane ratio ($C_2H_4/C_2H_6$) serves as an important indicator of OCM selectivity; a higher ratio reflects more efficient conversion to the desired product, ethylene. Optimizing this ratio through reaction parameters is key to maximizing ethylene yield while minimizing undesired by-products [46,47].

As shown in Fig. 3a, LCO exhibited stable methane conversion and product distribution over 15 h of time on stream (TOS), indicating good catalytic. The generated products at 850 °C were CO, $CO_2$, $C_2H_4$, $C_2H_6$, $C_3H_8$, and $C_4H_{10}$ in $O_2$-OCM. The $C_2$ products selectivity ($S_{C2}$) reached 41.5 %, corresponding to a $C_2$ production rate of 0.001 mol $g_{cat}^{-1}$ $min^{-1}$. The $C_2H_4/C_2H_6$ ratio was 2.16, suggesting a preference for ethylene production over ethane. The selectivities for the remaining products were 3.1 %, 13.2 %, and 42.2 % for $C_{3+}$, CO, and $CO_2$, respectively, with a methane conversion ($X_{CH4}$) of 18.6 %. These results are consistent with previously reported performances for LCO catalysts [48,49].

When $H_2O$ was used as the oxidant (Fig. 3b), LCO again showed stable performance over time, though the $CH_4$ conversion was significantly reduced ($X_{CH4}$ = 4.1 %). It can be explained by the low oxidation potential of $H_2O$ compared to $O_2$. Unlike the $O_2$-OCM, hydrogen was observed as the main product ($S_{H2}$ = 61.1 %). No $C_{3+}$ hydrocarbons were detected. The selectivities for CO and $CO_2$ were 16.4 %, and 17.9 %, respectively. $C_2$ selectivity was 4.6 %, corresponding to a $C_2$ production rate of ~0.0001 mol $g_{cat}^{-1}$ $min^{-1}$. The $C_2H_4/C_2H_6$ ratio of 0.7 suggests that the $C_2H_6$ to $C_2H_4$ dehydrogenation step was limited under these conditions.

Supported by our experimental results – including Raman spectra indicating oxygen vacancies and electrophilic surface oxygen species (Fig. 2b), as well the product selectivities in the catalytic test – we propose the following $H_2O$-OCM surface mechanism for oxide catalysts: (i) water molecules interact with oxygen vacancies ($V_o^{\cdot\cdot}$) and lattice oxygens ($O_o^x$) on the oxide surface forming hydroxide ions in the oxygen lattice position ($OH_o^{\cdot}$):

$$V_o^{\cdot\cdot} + O_o^x + H_2O \rightarrow 2OH_o^{\cdot} \quad \text{(R9)}$$

Then, (ii) $OH_o^{\cdot}$ species participate in the activation of $CH_4$ by C-H cleavage, leading to the formation of $C_2$ hydrocarbons and $H_2$:

$$2CH_4 + 2OH_o^{\cdot} \rightarrow C_2H_6 + H_2O + H_2 + V_o^{\cdot\cdot} + O_o^x \quad \text{(R10)}$$

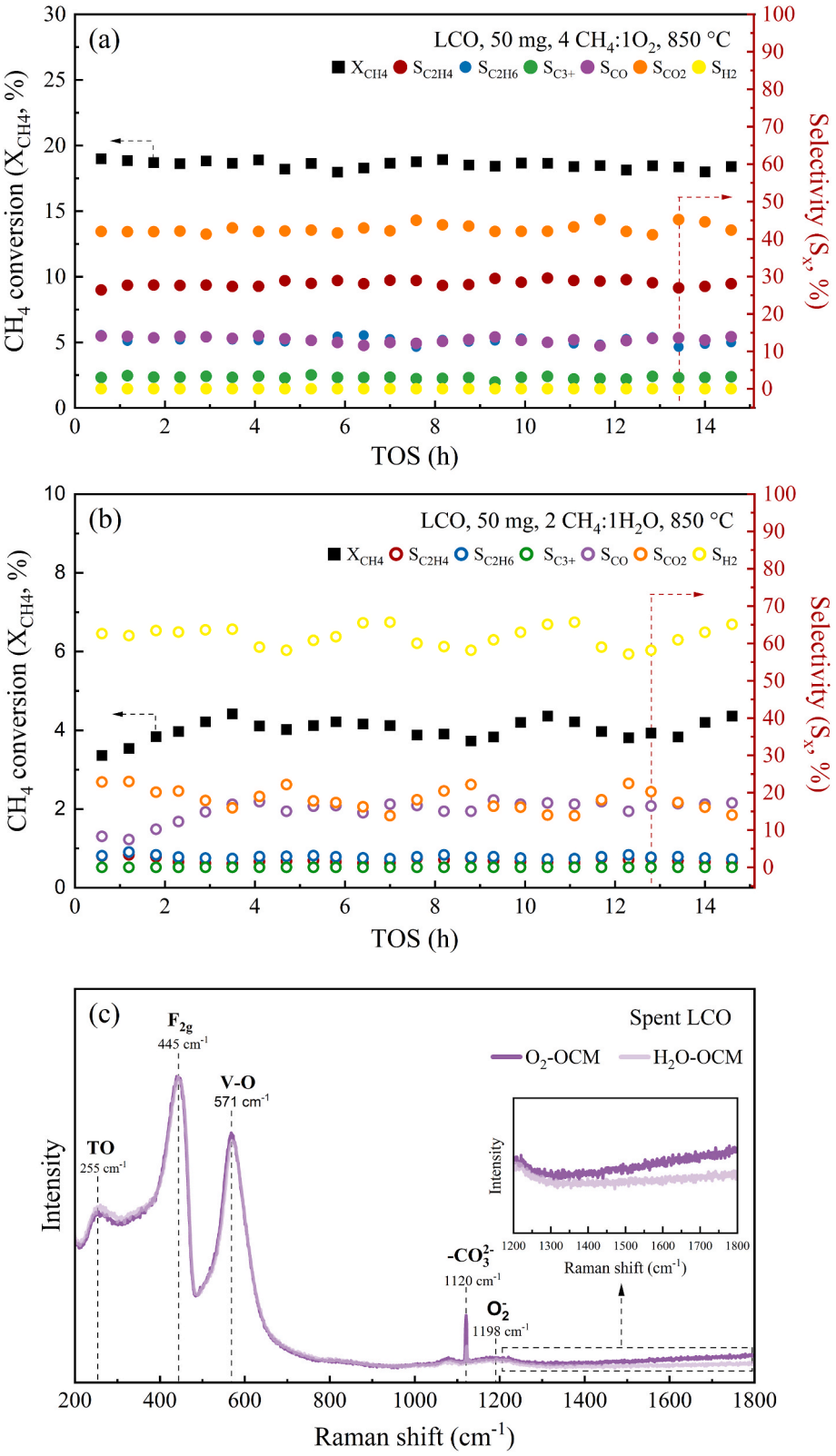


**Fig. 3.** OCM reactions with the $La_{0.5}Ce_{0.5}O_{2-\delta}$ catalyst. Effect of time on stream (TOS) on $CH_4$ conversion ($X_{CH4}$, left axis), and product selectivity ($S_x$, right axis) distribution for (a) **$O_2$-OCM** ($4CH_4$:$1O_2$), and (b) **$H_2O$-OCM** ($2CH_4$:$1H_2O$). Reactional conditions: 850 °C, 50 mg of catalyst, 60 mL $min^{-1}$ gas feed. $C_{3+} = C_3H_8 + C_4H_{10}$. (c) Raman spectroscopy of spent catalysts after ~15 h of each OCM reaction.

$$2CH_4 + 2OH_o^{\cdot} \rightarrow C_2H_4 + H_2O + 2H_2 + V_o^{\cdot\cdot} + O_o^x \quad (R11)$$

During this process, the catalyst surface is regenerated, allowing continuity of the reaction. It is important to note that the balanced reactions have the same stoichiometry of methane dehydrogenation (or dismutation) as demonstrated in Reactions 12 and 13.

$$2CH_4 \rightarrow C_2H_6 + H_2 \; \Delta H^0_{25^\circ C} = 64 \text{ kJ mol}^{-1} \quad (R12)$$

$$2CH_4 \rightarrow C_2H_4 + 2H_2 \; \Delta H^0_{25^\circ C} = 202 \text{ kJ mol}^{-1} \quad (R13)$$

The reaction Gibbs free energy ($\Delta G_r$) as a function of temperature for possible $CH_4$ conversion pathways – including the formation of $C_2$ hydrocarbons, CO, $CO_2$, and $H_2$ – using $H_2O$ and $O_2$ as oxidants, are shown in Fig. S2a and b, respectively. For methane conversion reactions with $H_2O$ (Fig. S2a), $\Delta G_r$s values are mostly positive in all temperature range (0–1200 °C), indicating limited thermodynamic favorability. Unless the WGS reaction (see orange line in Fig. S2a) which $\Delta G_r$ is negative at lower temperatures but becomes less favorable as temperature increases. Above 700 °C, SRM reaction becomes thermodynamically favorable, with $\Delta G_r$ values turning negative. For $H_2O$-OCM, the formation of $H_2$ and $CO_x$ is considered more favorable thermodynamically than that of $C_2$ products. However, the presence of oxygen vacancies resulting from the doping process and ceria redox properties, along with $H_2O$, can play a crucial role in lowering the energy barrier in Reactions 12 and 13, to favor $C_2$ formation. Aside from temperature, adding a stronger oxidant is another strategy to shift the thermodynamic equilibrium. When switching the oxidant to $O_2$ (Fig. S2b), the formation of $C_2$ becomes more favorable than the $H_2O$-OCM ones, with negative $\Delta G_r$ values across the evaluated temperature range. Therefore, the formation of deep oxidation products such as $CO_2$ is even more favorable, often resulting in reduced $C_2$ selectivity. Indeed, these thermodynamic tendencies have historically limited the industrial deployment of OCM due to the preferential formation of $CO_x$.

After the catalytic tests, the spent catalyst was analyzed by Raman spectroscopy (Fig. 3c). Graphitic carbon is typically identified by its characteristic D and G bands in the 1000–1800 $cm^{-1}$ region [50]. The G band (1500–1600 $cm^{-1}$) can be attributed to vibrational modes in all $sp^2$ (C=C) bonds in the rings and chains of ordered graphitic carbon, while the D band appears around 1300-1400 $cm^{-1}$ (D) and 1600–1630 $cm^{-1}$ (D'), reflecting disorder or crystallite size. The absence of these bands in Raman spectra (Fig. 3c) suggests that no carbon deposits were formed on the LCO catalyst during both OCM experiments.

Overall, LCO proved to be an effective catalyst for generating both value-added $C_2$ hydrocarbons and syngas-related products. Its thermochemical stability and compatibility with SOFC materials further support its application as a catalytic layer on the fuel electrode of a methane conversion-SOFC.

### 3.2. Characterization of the SOFC with LCO catalytic layer

It has been reported that a porous catalytic layer has a minor influence on the electrochemical behavior of the fuel cell running on hydrogen, while promoting great stability and activity for using carbon-containing fuels such as methane and ethanol. These preliminary results suggest the possibility of decoupling electrochemical and catalytic reactions in the fuel electrode, enabling further exploration of the methane conversion in SOFCs. Therefore, the LCO catalytic layer was applied to the fuel cell and tested for $CH_4$ conversion.

Fig. 4a shows cross-section SEM images of LCO catalytic layer deposited over the Ni/YSZ anode, evidencing good adhesion and compatible microstructure between the two layers after sintering at 900 °C. The catalytic layer, with a total thickness of ~21 μm resulting from 20 mg $cm^{-2}$ of LCO loading, displays a homogeneous and porous structure with average particle size of 0.50 ± 0.35 μm and ~40 % porosity. The anode layer thickness is ~41 μm, with uniform porosity (~45 %) and an average particle size of 0.85 ± 0.20 μm.

Initially, the single cell with the LCO catalytic layer was characterized under hydrogen (25 mL $min^{-1}$ of 10 % of $H_2$/He mixture), while the

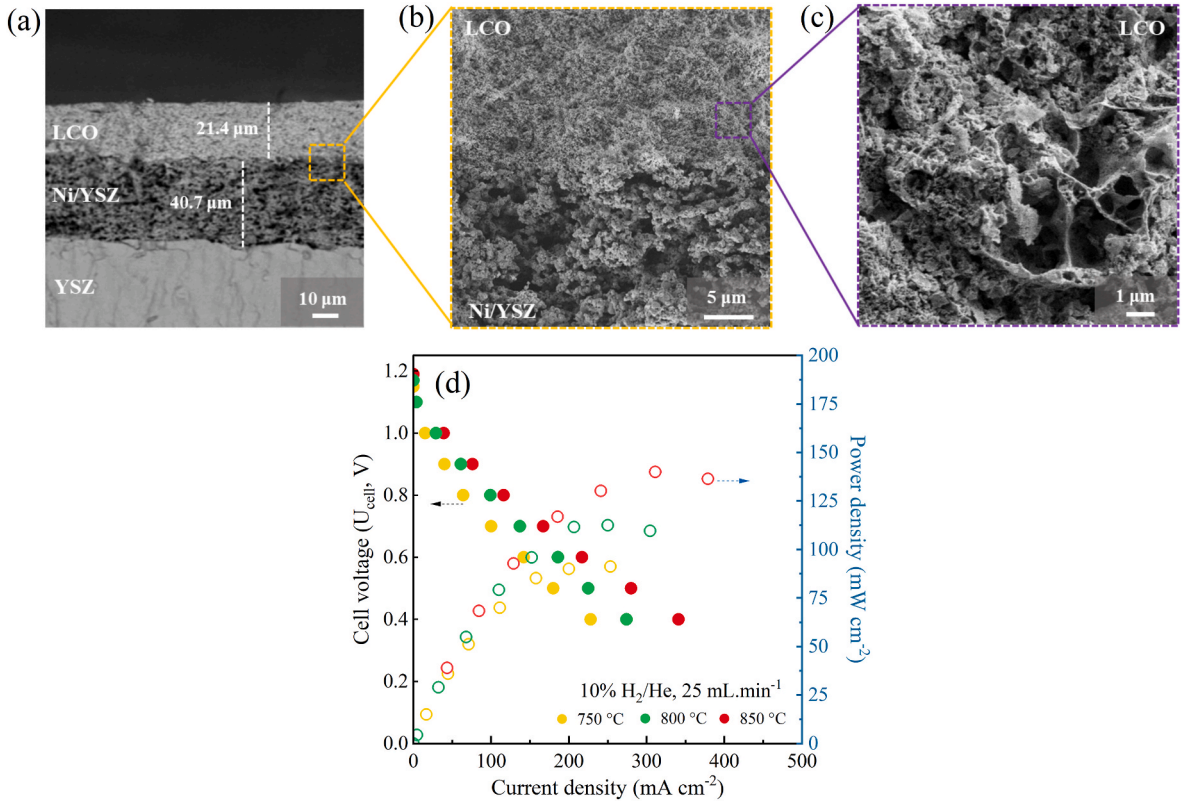


**Fig. 4.** SEM images of the SOFC with LCO catalytic layer before electrochemical tests: (a) fractured cross-section showing the anode side; (b) interface between catalytic layer and Ni/YSZ anode, and (c) magnified view of LCO layer. (d) i-V-P curves under $H_2$ of the LCO, Au, Ni-YSZ|YSZ|LSM fuel cell at 750, 800, and 850 °C.

cathode was fed with 90 mL $min^{-1}$ of synthetic air. The i-V-P curves measured at different temperatures are shown in Fig. 4b. The OCV remained stable between 1.13 and 1.19 V in the investigated temperature range. These values are close to the theoretical Nernst potential, indicating effective gas tightness. This confirms the absence of oxygen leakage from the cathode, which could otherwise influence the oxidative coupling reactions at the fuel electrode, as reported in previous OCM in SOFC studies [19]. The i-V curves demonstrate increasing currents and power density with increasing temperature. However, due to the thick electrolyte and the low operating temperature for the LSM cathode, the cell has a relatively low current density compared to the state-of-the-art anode-supported SOFCs [51]. Nonetheless, these features have no impact on the main goal of this study, which aims to investigate the methane conversion in the SOFC modified with an OCM catalyst.

### 3.3. Methane conversion in SOFC with LCO catalytic layer

The conversion of $CH_4$ and $C_2$ selectivity are significantly influenced by OCM reaction parameters, such as temperature, residence time, and oxygen concentration. Coupling both the electrochemical and catalytic methane reactions in the fuel electrode brings more complex reaction pathways that require a systematic characterization. Therefore, the effects of temperature, anode inlet flow rate, and generated current on $CH_4$ conversion were evaluated. After operating in hydrogen (Fig. 4b), this fuel was gradually switched to methane without the addition of external water/steam. Methane conversion in SOFC was thus carried out using only $H_2O$ generated by the anodic electrochemical reactions. At each operating condition, the cell voltage remained stable, and the product distribution was continuously monitored using online GC/MS analysis.

Preliminary $CH_4$ conversion tests were carried out using various $CH_4$ concentrations (10, 50, and 100 %) and current densities (i = 20 and 40 mA $cm^{-2}$) at 800 °C, as summarized in Table 1. In SOFC operation, the supply of oxidizing species at the anode side is controlled by the flux of oxygen ions ($O^{2-}$) electrochemically transported through the electrolyte from the cathode reduction reaction. The total $O^{2-}$-transfer flux (*j*) is directly proportional to the generated current (i), as defined by Faraday's law (Equation (3)).

$$j\ (\text{mol s}^{-1}\ \text{cm}^{-2}) = \text{i}/2\text{F} \quad \text{(Eq. 3)}$$

An inversed relationship between methane conversion and $C_2$ product selectivity distribution has been reported [52,53], where $S_{C2}$ sharply decreases while $CO_x$ formation increases when $X_{CH4}$ exceeds 10 %. Therefore, to achieve higher $C_2$ selectivity, it is essential to operate at low oxygen or oxidant partial pressure. Since the number of oxidizing species is directly determined by the current, the relationship between oxidant availability and methane feed can be expressed by the $O^{2-}/CH_4$ molar ratio descriptor. As expected, higher $X_{CH4}$ and lower $S_{C2}$ values were achieved with increasing $O^{2-}/CH_4$ ratio, while the reforming products ($H_2$ and CO) remained relatively unaffected. No $C_{3+}$ products were detected under the tested conditions, whereas the highest selectivities were for the reforming products. Notably, for equivalent $O^{2-}/CH_4$ ratios – whether achieved by adjusting current density or methane concentration – similar $X_{CH4}$ and product selectivity values were observed. Higher $O^{2-}/CH_4$ ratios (>0.012) showed a slight increase in $S_{CO2}$, while $S_{C2}$ declined (Table 1). These results are in agreement with the fixed-bed catalytic behavior of LCO and the presence of electrochemically generated water at the anode.

Given that the main purpose of this study is to investigate the production of $C_2$ hydrocarbons, experiments were focused on $O^{2-}/CH_4$ ratios of 0.006 and 0.012 to explore how operating parameters influence product distribution. Low current densities were selected to keep deficient concentration of oxidant species and avoid deeper oxidation reactions.

To further assess the effects of operating conditions on the complex reactions taking place at the fuel electrode and optimize $C_2$ selectivity, additional tests were conducted at a constant polarization of 20 mA $cm^{-2}$. Reaction temperatures of 750, 800, and 850 °C were evaluated within a safe measurement range to ensure seal integrity. Both methane concentration and residence time were kept at 50 % $CH_4$/He and a flow rate of 50 mL $min^{-1}$, respectively ($O^{2-}/CH_4$ = 0.006). As shown in Fig. 5a, the electrochemical reactor performance was strongly dependent on the temperature. Increasing the operating temperature leads to a sharp increase of both $X_{CH4}$ and $S_{C2}$. At 750 °C, $X_{CH4}$ was 2 % and $S_{C2}$ of 6 %, while at 850 °C, $X_{CH4}$ and $S_{C2}$ values reached 5 % and 17 %, respectively.

Additionally, an increase in the $C_2H_4/C_2H_6$ ratio was observed (Fig. 5b). This suggests enhanced ethylene formation through gas-phase ethane dehydrogenation, a process typically favored at temperatures 50–100 °C higher than those required for surface dehydrogenation reactions [54]. These findings highlight that elevated temperatures promote gas-phase reactions such as methyl radical formation (Reaction 14) and thermal dehydrogenation of $C_2H_6$ to $C_2H_4$ (Reaction 15) [55,56], thereby improving overall selectivity toward $C_2$ products, with a maximum production rate of $C_2$ = 1470 μmol $min^{-1}$ $cm^{-2}$.

$$CH_4 + H^{\bullet} \leftrightarrow {}^{\bullet}CH_3 + H_2 \quad \text{(R14)}$$

$${}^{\bullet}CH_3 + {}^{\bullet}CH_3 \leftrightarrow C_2H_6 \leftrightarrow {}^{\bullet}C_2H_5 + H^{\bullet} \leftrightarrow C_2H_4 + H^{\bullet} \quad \text{(R15)}$$

Notably, at 850 °C, a small fraction of $C_3$ (~1 %) was detected, indicating that higher temperatures favor coupling and chain elongation reactions (Reaction 16).

$${}^{\bullet}CH_3 + {}^{\bullet}C_2H_5 \leftrightarrow C_3H_8 \quad \text{(R16)}$$

As the formation of $C_2$ hydrocarbons is highly dependent on the coupling of intermediates and radicals in the gas phase, the residence time is a key parameter to investigate within the methane conversion-SOFC. To evaluate this, experiments were performed at varying anode inlet flow rates (10, 25, and 50 mL $min^{-1}$) while keeping all other parameters fixed (Fig. 6). $X_{CH4}$ decreased significantly with increasing flow rate, dropping from 22 % at 10 mL $min^{-1}$ to 4 % at 50 mL $min^{-1}$. This behavior is anticipated because the electric current was kept constant across the different flow rates. Conversely, both $C_2$ selectivity and production rate increased by increasing the fuel flow rate (or decreasing the residence time) at the expense of $CO_2$ and $H_2$ production (Fig. 6a). Similar trends have been reported for electrocatalytic anodes in electrochemical OCM reactors [57,58]. At low flow rates, mass transfer limitations can become significant and hinder the access of methane to

**Table 1**
Summary of experimental investigation of $O^{2-}/CH_4$ ratio variation in the methane conversion SOFC-reactor at 800 °C. The $CH_4$ inlet flow was balanced in He.

| Temp. (°C) | Anode inlet (mL $min^{-1}$) | $[CH_4]_{inlet}$ (%) | i (mA $cm^{-2}$) | $O^{2-}/CH_4$ ratio | $X_{CH4}$ (%) | Selectivity (%) | | | |
|---|---|---|---|---|---|---|---|---|---|
| | | | | | | $C_2$ | $H_2$ | CO | $CO_2$ |
| 800 | 25 | 10 | 20 | 0.06 | 32 | 1 | 48 | 50 | 1 |
| 800 | 25 | 50 | 20 | 0.012 | 10 | 7 | 50 | 42 | 1 |
| 800 | 25 | 100 | 20 | 0.006 | 6 | 9 | 42 | 47 | 2 |
| 800 | 25 | 10 | 40 | 0.12 | 38 | 1 | 46 | 51 | 2 |
| 800 | 25 | 50 | 40 | 0.024 | 15 | 3 | 48 | 47 | 2 |
| 800 | 25 | 100 | 40 | 0.012 | 10 | 5 | 46 | 46 | 3 |
| 800 | 50 | 100 | 20 | 0.006 | 3 | 10 | 53 | 36 | 1 |

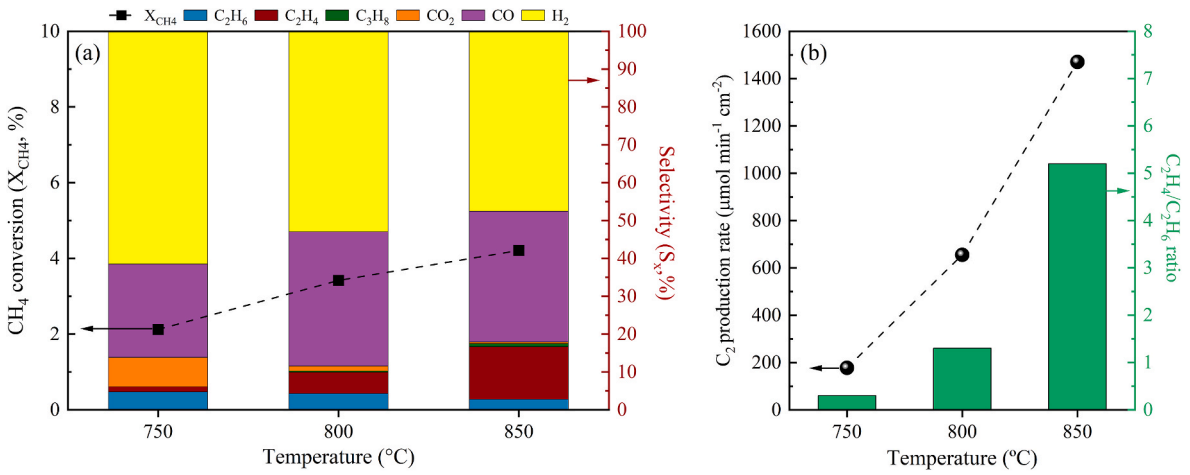


**Fig. 5.** (a) Methane conversion and product selectivity, and (b) $C_2$ production rate and $C_2H_4/C_2H_6$ ratio as a function of temperature for the methane conversion-SOFC operating at 750, 800, and 850 °C. Reactional conditions: anode flow of 50 mL $min^{-1}$ with 50 % $CH_4$/He and 20 mA $cm^{-2}$.

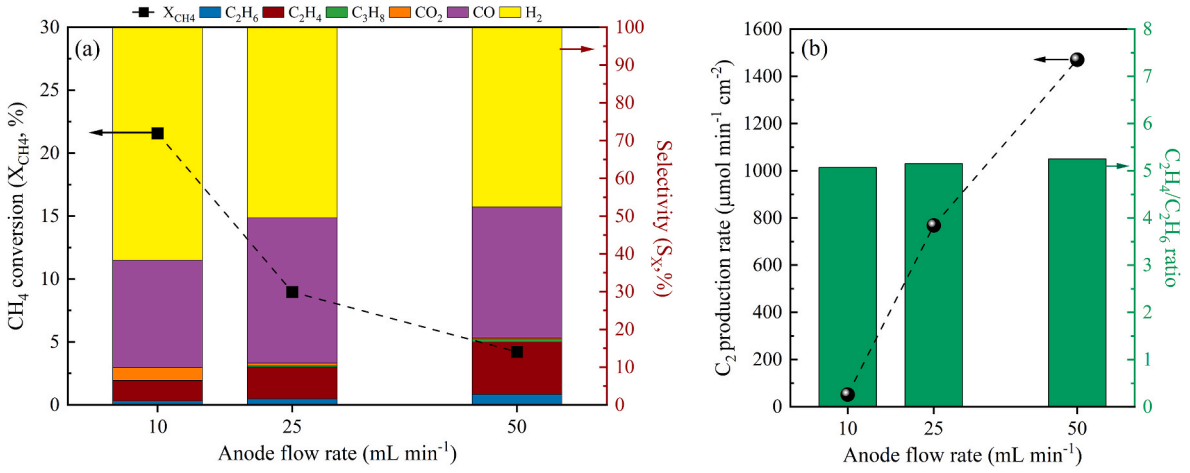


**Fig. 6.** (a) Distribution of product selectivity for the methane conversion-SOFC under different anode inlet flow rates (10, 25, and 50 mL $min^{-1}$) with 50 % $CH_4$/He, and (b) $C_2$ production rate and $C_2H_4/C_2H_6$ ratio as a function of anode flow rate. Reactional conditions: 20 mA $cm^{-2}$ at 850 °C.

the catalytic sites for its activation into methyl radicals. Nonetheless, the most pronounced effect was the marked increase in $C_2$ production rate from ~50 to 1500 μmol $min^{-1}$ $cm^{-2}$ (Fig. 6b) achieved at 50 mL $min^{-1}$. The $C_2H_4/C_2H_6$ ratio is practically unaffected by changes in flow rate (Fig. 6b), suggesting that $C_2H_4$ is predominantly formed through the thermal dehydrogenation route (R15), independent of mass transfer processes between the catalyst surface and the gas phase.

Polarizations experiments were conducted at current densities of 20, 40, and 100 mA $cm^{-2}$ with a 50 % $CH_4$/He anode inlet (50 mL $min^{-1}$) at 850 °C, as shown in Fig. 7. The cell voltage at each polarization remained practically constant during ~2.5 h of reaction, indicating good system stability. As expected, increasing the electric current led to

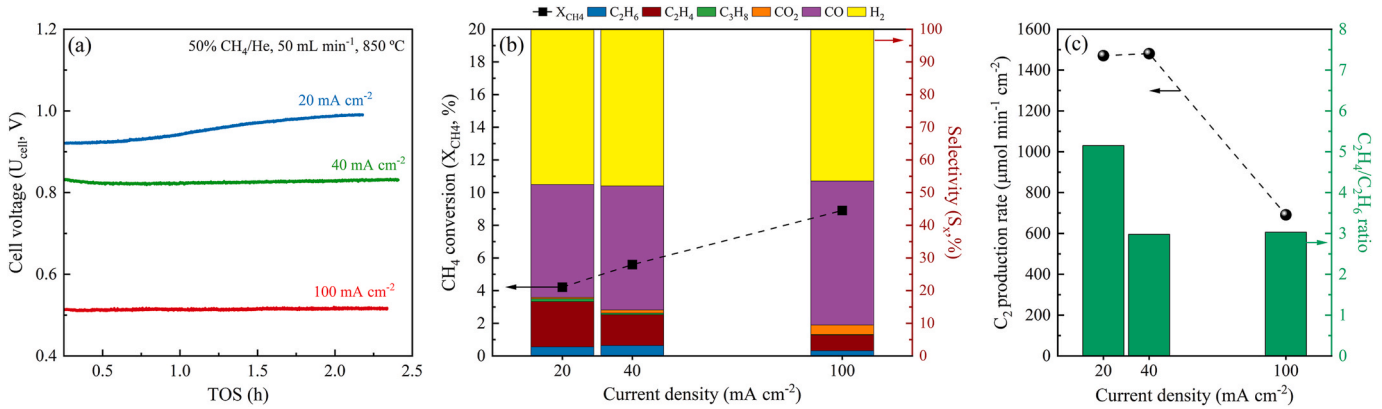


**Fig. 7.** (a) Cell voltage as a function of TOS. (b) Methane conversion and product selectivity for the methane conversion-SOFC under different polarizations (20, 40, and 100 mA $cm^{-2}$). (c) $C_2$ production rate and $C_2H_4/C_2H_6$ ratio as a function of generated current density. Reactional conditions: anode inlet of 50 mL $min^{-1}$ with 50 % $CH_4$/He at 850 °C.

higher $X_{CH4}$ values (Fig. 7b), since fuel utilization rate must increase to generate more current. Consequently, this also increases the concentration of oxidizing species at the anode. Intermediary currents densities of 20 and 40 mA $cm^{-2}$ resulted in the highest $C_2$ selectivity values, $S_{C2}$ = 17 % and 13 %, respectively. At such currents, the $C_2$ production rate reached ~1500 μmol $min^{-1}$ $cm^{-2}$. The most favorable condition for obtaining ethylene was observed at 20 mA $cm^{-2}$, achieving the highest $C_2H_4/C_2H_6$ ratio of 5 (Fig. 7c). At higher $CH_4$ conversions, the total oxidation reactions are favored, a behavior commonly observed in OCM and previously discussed [22,24]. $CO_2$ selectivity was 0.5 %, 1 %, and 3 % for i = 20, 40, and 100 mA $cm^2$, respectively. Alongside $C_2$, $H_2$ and CO were the major products, with $S_{H2}$ = 48 % and $S_{CO}$ = 35 % at i = 20 mA $cm^{-2}$. These results indicate that syngas is a primary product of the combined electrochemical and catalytic processes occurring within the fuel electrode (comprising both the anode and the LCO catalytic layer).

The observed production of syngas with an $H_2$/CO ratio of ~1.4

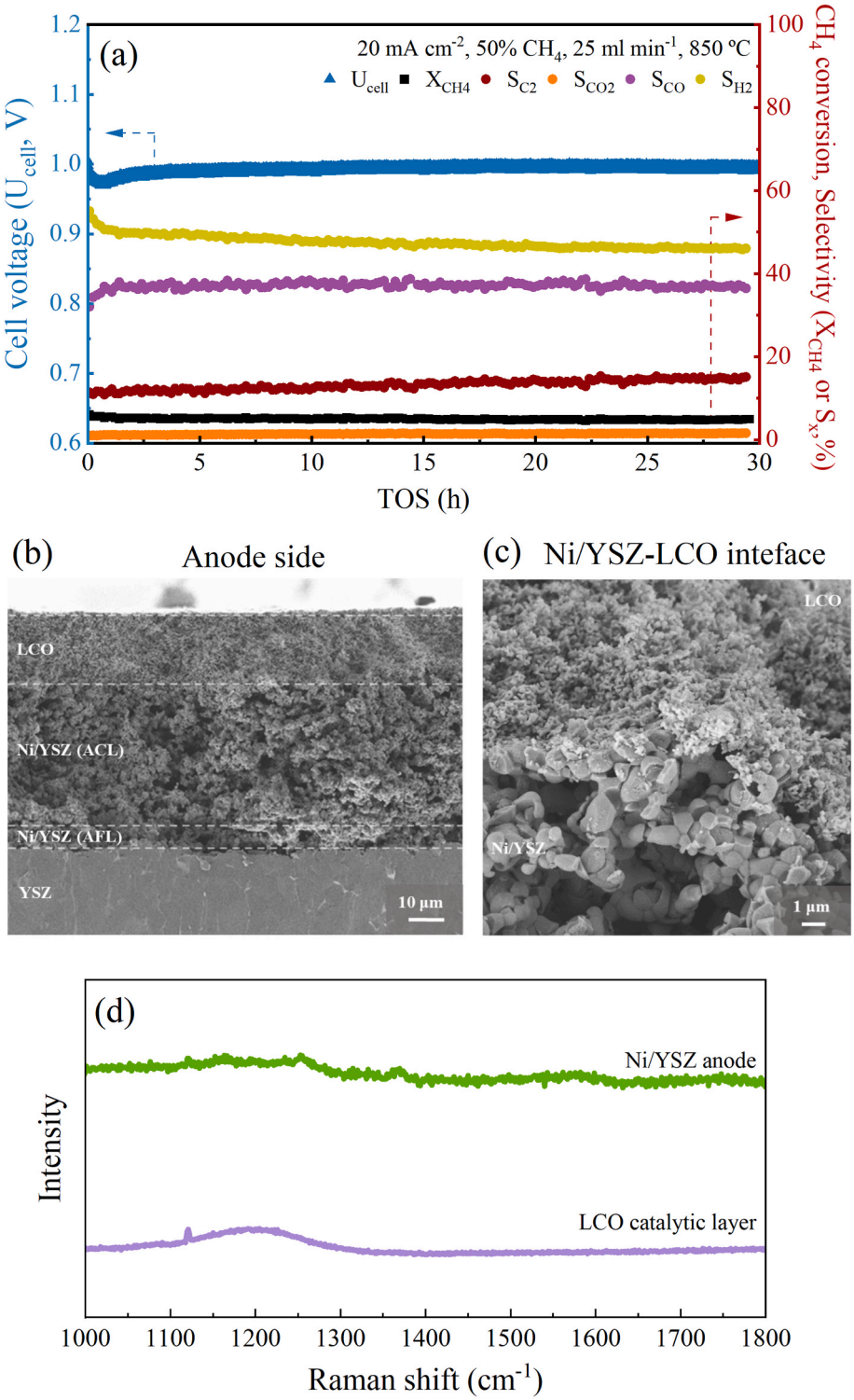


**Fig. 8.** (a) Methane conversion in SOFC with LCO catalytic layer: cell voltage, $CH_4$ conversion, and product selectivity as a function of TOS. Reaction conditions: 50 % $CH_4$/He anode inlet of 25 mL $min^{-1}$, 20 mA $cm^{-2}$ of generated current at 850 °C. Post-test characterization of the SOFC after operation under $CH_4$: cross-sectional SEM images of (b) fuel electrode side and (c) anode/catalytic layer interface; and (d) Raman spectra for the LCO catalytic layer and Ni/YSZ anode (ACL).

suggests a significant contribution from SRM reaction (R1) in the studied SOFC configuration, consistent with the favorable thermodynamics of this reaction over the coupling reactions under the experimental conditions [59]. SRM is likely to take place in the catalytic layer with the $H_2O$ arising from $H_2$ electrochemical oxidation of $H_2$ in the anodic triple phase boundary (TPB) [46,60]. Previous studies utilizing SOFCs with a single anode material configuration that is simultaneously active for both electrochemical and coupling reactions also reported the formation of reforming products in addition to $C_2$ products [54,58,61].

In the present SOFC configuration, with the catalytic layer, $CH_4$ is not directly oxidized by the electrochemically pumped $O^{2-}$ ions to the anode (as illustrated in Fig. 1). Instead, these ions participate in the electrochemical oxidation of $H_2$ at the Ni/YSZ anode. The resulting $H_2O$ interacts with the LCO surface, which structural defects promote the dissociative adsorption of $H_2O$ molecules (see Section 3.1). This process may result in the creation of surface mobile species ($OH_o$), which can participate in methyl radical formation. This hypothesis is supported by similarities in both conversion and product distribution found in methane conversion-SOFC and $H_2O$-OCM fixed bed test results (Fig. 3b). The stability of this SOFC configuration depends on the OCM catalyst, internal reforming, and electrochemical reactions. Incorporating a catalytic layer benefits from the separation between catalytic and electrochemical reactions, enabling a synergistic combination of reactions that support each other to produce value-added chemicals and power cogeneration.

To evaluate the short-term stability of the SOFC with LCO catalytic layer, a 30-h methane conversion test was performed. Fig. 8a presents the time on stream evolution of cell voltage, methane conversion, and product selectivity, all of which remained stable throughout the experiment. Single cell post-test characterization was conducted by SEM and Raman spectroscopy (Fig. 8b–d). SEM images of the interfaces between the catalytic layer, anode, and electrolyte (Fig. 8b) revealed good compatibility and adhesion, with no signs of delamination or cracking. The LCO layer microstructure remained similar to that of the fresh cell (see Fig. 4a–c), and no carbon deposition was observed (Fig. 8c). Raman analysis further confirmed the absence of carbon deposits, as no D or G bands associated with disordered or graphitic carbon were detected in either the LCO layer or the Ni/YSZ anode (Fig. 8d). A comparison of the Raman spectra of the post-test LCO catalytic layer and the as-prepared powder (Fig. S3) demonstrated the structural stability of the catalyst after prolonged high-temperature operation in the SOFC reactor.

The deactivation of SOFC due to coking and methane utilization has been previously reported [62,63]. Stable operation of SOFCs directly fueled with dry $CH_4$ without a catalytic layer is achieved at high methane utilization levels when enough steam is generated to sustain SRM reaction. However, when methane utilization is below ~13 %, a decline in current density occurs and the SOFC rapidly deactivates due to carbon deposition over the Ni/YSZ anode. The catalytic layer has been found to extend the working window for stable performance under direct methane conditions [62].

In the present study, the tests were carried out at low fuel utilization (~4–10 %), a regime that is likely to promote methane decomposition (R6) or deep oxidation at the Ni-based anode, leading to coke or $CO_2$ formation. However, the absence of carbon deposits and the low $CO_2$ selectivity ($S_{CO2}$ ~1–4 %) suggest that the LCO catalytic layer effectively promotes $CH_4$ conversion while serving as a barrier that prevents methane from reaching the Ni particles.

## 4. Conclusions

$La_{0.5}Ce_{0.5}O_{2-\delta}$ catalyst was found to be active for the oxidative coupling of methane reaction, using both $O_2$ or $H_2O$ as oxidants. Furthermore, the reaction mechanism for $H_2O$-OCM was proposed. The YSZ electrolyte-supported solid oxide fuel cell was modified with a $La_{0.5}Ce_{0.5}O_{2-\delta}$ catalytic layer added to Ni/YSZ anode for direct $CH_4$ operation, aiming at the production of value-added chemicals. The combined catalytic and electrochemical reactions resulted in the formation of both oxidative coupling and reforming products, being syngas the primary product. $C_2$ selectivity was proved to be sensitive to key operating parameters, such as $O^{2-}/CH_4$ molar ratio, anode inlet flow rate, generated current, and temperature. Increasing the operating temperature to 850 °C favored $CH_4$ conversion and $C_2$ selectivity, reaching a maximum $C_2$ product selectivity of 1.5 mmol $min^{-1}$ $cm^{-2}$ and over 50 % selectivity for syngas ($H_2/CO$ ~ 1). In contrast, higher generated current densities enhanced $CH_4$ conversion but suppressed $C_2$ hydrocarbons formation. The SOFC with the LCO catalytic layer showed a stable performance by the association of electrochemical hydrogen oxidation and the thermocatalytic reactions of methane steam reforming and methane oxidative coupling. Adjusting the SOFC operating parameters allows controlling intricate reaction pathways in the catalytic layer and anode. These findings illustrate an innovative approach to cogenerating syngas, $C_2$ hydrocarbons, and electrical power in a SOFC reactor with a tailored catalytic layer that can be tuned to prevent carbon deposition. In summary, this study highlights the versatility of SOFCs as an electrochemical reactor that can couple a compatible catalytic active material to provide a promising pathway for sustainable and economically viable production of chemicals from abundant $CH_4$ feedstocks with a surplus of energy.

## CRediT authorship contribution statement

**Vanessa B. Vilela:** Writing – original draft, Visualization, Methodology, Investigation, Formal analysis, Data curation. **Franck Fournet-Fayard:** Formal analysis. **Marlu C. Steil:** Writing – review & editing, Supervision, Resources, Project administration, Funding acquisition, Conceptualization. **Vivian V. Thyssen:** Writing – review & editing, Investigation, Formal analysis. **Daniel Z. de Florio:** Investigation, Formal analysis. **Andre S. Ferlauto:** Writing – review & editing, Investigation, Formal analysis. **Fabio C. Fonseca:** Writing – review & editing, Supervision, Resources, Project administration, Funding acquisition, Conceptualization.

## Declaration of competing interest

The authors declare that they have no known competing financial interests or personal relationships that could have appeared to influence the work reported in this paper.

## Acknowledgment

This work was supported by the Brazilian agencies CNEN, CNPq (SisH2 407967/2022-2 and 403015/2024-03), FAPESP (2024/19207-9 and 2023/14931-8), and Center for Innovation on New Energies (CINE) - SHELL (ANP) / FAPESP (2017/11937- 4). This research has benefited from the characterization equipment of the Grenoble INP – CMTC platform supported by the Centre of Excellence of Multifunctional Architectured Materials *"CEMAM'' (ANR-10-LABX-44-01)*. The authors would also like to thank Prof. J. Fouletier (LEPMI - Grenoble INP, UGA) for many useful discussions and the critical reading of the manuscript. ASF and FCF are fellows of the CNPq.

## Appendix A. Supplementary data

Supplementary data to this article can be found online at https://doi.org/10.1016/j.jpowsour.2025.238083.

## Data availability

Data will be made available on request.

## References


[1] International Energy Agency - IEA, World energy outlook 2022. www.iea.org/reports/world-energy-outlook-2022, 2022. (Accessed 7 December 2024).

[2] P. Schwach, X. Pan, X. Bao, Direct conversion of methane to value-added chemicals over heterogeneous catalysts: challenges and prospects, Chem. Rev. 117 (2017) 8497–8520, https://doi.org/10.1021/acs.chemrev.6b00715.

[3] J.H. Lunsford, Catalytic conversion of methane to more useful chemicals and fuels: a challenge for the 21st century, Catal. Today 63 (2000) 165–174, https://doi.org/10.1016/S0920-5861(00)00456-9.

[4] G. Keller, M. Bhasin, Synthesis of ethylene via oxidative coupling of methane, J. Catal. 73 (1982) 9–19, https://doi.org/10.1016/0021-9517(82)90075-6.

[5] X. Meng, X. Cui, N.P. Rajan, L. Yu, D. Deng, X. Bao, Direct methane conversion under mild condition by Thermo-, Electro-, or photocatalysis, Chem 5 (2019) 2296–2325, https://doi.org/10.1016/j.chempr.2019.05.008.

[6] C.-G. Zhan, J.A. Nichols, D.A. Dixon, Ionization potential, electron affinity, electronegativity, hardness, and electron excitation energy: molecular properties from density functional theory orbital energies, J. Phys. Chem. A 107 (2003) 4184–4195, https://doi.org/10.1021/jp0225774.

[7] A. Cruellas, J.J. Bakker, M. van Sint Annaland, J.A. Medrano, F. Gallucci, Techno-economic analysis of oxidative coupling of methane: current state of the art and future perspectives, Energy Convers. Manag. 198 (2019) 111789, https://doi.org/10.1016/j.enconman.2019.111789.

[8] P.V.L. Reddy, K.-H. Kim, H. Song, Emerging green chemical technologies for the conversion of CH4 to value added products, Renew. Sustain. Energy Rev. 24 (2013) 578–585, https://doi.org/10.1016/j.rser.2013.03.035.

[9] C. Zhu, S. Hou, X. Hu, J. Lu, F. Chen, K. Xie, Electrochemical conversion of methane to ethylene in a solid oxide electrolyzer, Nat. Commun. 10 (2019) 1173, https://doi.org/10.1038/s41467-019-09083-3.

[10] P. De Luna, C. Hahn, D. Higgins, S.A. Jaffer, T.F. Jaramillo, E.H. Sargent, What would it take for renewably powered electrosynthesis to displace petrochemical processes? Science (1979) 364, https://doi.org/10.1126/science.aav3506, 2019.

[11] E. Antolini, Low molecular weight alkane-fed solid oxide fuel cells for power and chemicals cogeneration, J. Energy Chem. 80 (2023) 711–735, https://doi.org/10.1016/j.jechem.2023.01.033.

[12] V.V. Thyssen, V.B. Vilela, D.Z. De Florio, A.S. Ferlauto, F.C. Fonseca, Direct conversion of methane to C2 hydrocarbons in solid-state membrane reactors at high temperatures, Chem. Rev. 122 (2022) 3966–3995, https://doi.org/10.1021/acs.chemrev.1c00447.

[13] G. Marnellos, M. Stoukides, Catalytic studies in electrochemical membrane reactors, Solid State Ionics 175 (2004) 597–603, https://doi.org/10.1016/j.ssi.2004.03.038.

[14] N.U. Pujare, A.F. Sammells, Methane activation to C2 hydrocarbon species in solid oxide fuel cell, J. Electrochem. Soc. 135 (1988) 2544–2545, https://doi.org/10.1149/1.2095375.

[15] M.A. Buccheri, A. Singh, J.M. Hill, Anode- versus electrolyte-supported Ni-YSZ/YSZ/Pt SOFCs: effect of cell design on OCV, performance and carbon formation for the direct utilization of dry methane, J. Power Sources 196 (2011) 968–976, https://doi.org/10.1016/j.jpowsour.2010.08.073.

[16] Y. He, F. Meng, G. Xing, K. Liu, S. Lou, H. Xiao, Y. Tang, Direct oxidative coupling of methane into ethylene in a catalyst-enhanced planar solid oxide fuel cell stack reactor, Phy. Open 20 (2024) 100219, https://doi.org/10.1016/j.physo.2024.100219.

[17] R. Wang, T. Wang, Y. Ma, T. Wei, Z. Ye, B. Chen, D. Dong, Control of carbon deposition over methane-fueled SOFCs through tuning the O/C ratio at the anode/electrolyte interface, J. Power Sources 544 (2022) 231854, https://doi.org/10.1016/j.jpowsour.2022.231854.

[18] K. Otsuka, K. Suga, I. Yamanaka, Electrochemical control for oxidative coupling of methane over LiNiO2 using solid electrolytes, Chem. Lett. 17 (1988) 317–318, https://doi.org/10.1246/cl.1988.317.

[19] Z. Liu, T. He, W. Chen, D. Zhang, X. Xu, J. Wu, Co-Generation of electricity and chemicals via solid oxide fuel cells using Li-Doped LSGM and LSF composite anodes, Energy Fuels 37 (2023) 3091–3101, https://doi.org/10.1021/acs.energyfuels.2c03875.

[20] X. Xu, H. Li, X. Han, Y. Zheng, Enhancing electrochemical methane coupling in solid oxide cells by tuning oxygen species in the catalyst, J. Mater. Chem. A Mater. 12 (2024) 5115–5123, https://doi.org/10.1039/D3TA07648B.

[21] L.H. Denoyer, A. Benavidez, F.H. Garzon, K.P. Ramaiyan, Highly stable doped barium niobate based electrocatalysts for effective electrochemical coupling of methane to ethylene, Adv. Mater. Interfac. 9 (2022) 2200796, https://doi.org/10.1002/admi.202200796.

[22] K. Liu, J. Zhao, D. Zhu, F. Meng, F. Kong, Y. Tang, Oxidative coupling of methane in solid oxide fuel cell tubular membrane reactor with high ethylene yield, Catal. Commun. 96 (2017) 23–27, https://doi.org/10.1016/j.catcom.2017.03.010.

[23] W. Appamana, S. Charojrochkul, S. Assabumrungrat, W. Wiyaratn, Synthesis of Na2WO4-Mn supported YSZ as a potential anode catalyst for oxidative coupling of methane in SOFC reactor, Eng. J. 19 (2015) 13–20, https://doi.org/10.4186/ej.2015.19.1.13.

[24] T. Tagawa, K.K. Moe, M. Ito, S. Goto, Fuel cell type reactor for chemicals-energy co-generation, Chem. Eng. Sci. 54 (1999) 1553–1557, https://doi.org/10.1016/S0009-2509(99)00050-0.

[25] G. Xiu-Mei, K. Hidajat, C.B. Ching, C. Hong-Fang, Oxidative coupling of methane in solid oxide fuel cells, Stud. Surf. Sci. Catal. 110 (1997) 683–692, https://doi.org/10.1016/s0167-2991(97)81030-0.

[26] Z. Zhan, S.A. Barnett, Use of a catalyst layer for propane partial oxidation in solid oxide fuel cells, Solid State Ionics 176 (2005) 871–879, https://doi.org/10.1016/j.ssi.2004.12.005.

[27] M. Machado, L.N. Rodrigues, V.B. Vilela, T.S. Moraes, A.S. Ferlauto, F.C. Fonseca, Shape control of ceria catalytic supports for enhanced ethanol reforming in solid oxide fuel cells, ACS Appl. Energy Mater. 7 (2024) 1766–1776, https://doi.org/10.1021/acsaem.3c02757.

[28] M.C. Steil, S.D. Nobrega, S. Georges, P. Gelin, S. Uhlenbruck, F.C. Fonseca, Durable direct ethanol anode-supported solid oxide fuel cell, Appl. Energy 199 (2017) 180–186, https://doi.org/10.1016/j.apenergy.2017.04.086.

[29] S.D. Nobrega, P. Gelin, S. Georges, M.C. Steil, B.L. Augusto, F.B. Noronha, F. C. Fonseca, A fuel-flexible solid oxide fuel cell operating in gradual internal reforming, J. Electrochem. Soc. 161 (2014) F354–F359, https://doi.org/10.1149/2.107403jes.

[30] P. Zhang, L. Hu, B. Zhao, Z. Lei, B. Ge, Z. Yang, X. Jin, S. Peng, Direct power generation from ethanol by solid oxide fuel cells with an integrated catalyst layer, Fuel 333 (2023) 126340, https://doi.org/10.1016/J.FUEL.2022.126340.

[31] X. Li, K. Tomishige, K. Fujimoto, Oxidative coupling of methane by water as the oxidant on perovskite oxide catalysts, Catal. Lett. 36 (1996) 21–24, https://doi.org/10.1007/BF00807200.

[32] A.M. Arinaga, M.C. Ziegelski, T.J. Marks, Alternative oxidants for the catalytic oxidative coupling of methane, Angew. Chem., Int. Ed. 60 (2021) 10502–10515, https://doi.org/10.1002/anie.202012862.

[33] I. Hussain, G. Tanimu, S. Ahmed, C.U. Aniz, H. Alasiri, K. Alhooshani, A review of the indispensable role of oxygen vacancies for enhanced CO2 methanation activity over CeO2-based catalysts: uncovering, influencing, and tuning strategies, Int. J. Hydrogen Energy 48 (2023) 24663–24696, https://doi.org/10.1016/j.ijhydene.2022.08.086.

[34] M. Boscherini, A. Storione, M. Minelli, F. Miccio, F. Doghieri, New perspectives on catalytic hydrogen production by the reforming, partial oxidation and decomposition of methane and biogas, Energies 16 (2023) 6375, https://doi.org/10.3390/en16176375.

[35] Z.Q. Wang, D. Wang, X.Q. Gong, Strategies to improve the activity while maintaining the selectivity of oxidative coupling of methane at La2O3: a density functional theory study, ACS Catal. 10 (2020) 586–594, https://doi.org/10.1021/acscatal.9b03066.

[36] X. Zhou, Y. Pang, Z. Liu, E.I. Vovk, A.P. van Bavel, S. Li, Y. Yang, Active oxygen center in oxidative coupling of methane on La2O3 catalyst, J. Energy Chem. 60 (2021) 649–659, https://doi.org/10.1016/j.jechem.2021.01.008.

[37] B. Choudhary, L. Besra, S. Anwar, S. Anwar, La2Ce2O7 based materials for next generation proton conducting solid oxide cells: progress, opportunity and future prospects, Int. J. Hydrogen Energy 48 (2023) 28460–28501, https://doi.org/10.1016/j.ijhydene.2023.03.393.

[38] V.B. Vilela, V.V. Thyssen, L.N. Rodrigues, F.C. Fonseca, Enhancing the catalytic activity of lanthanum-ceria fluorite for methane conversion in SOFC, ECS Trans. 103 (2021) 1917–1925, https://doi.org/10.1149/10301.1917ecst.

[39] A.A.A. da Silva, M.C. Steil, F.N. Tabuti, R.C. Rabelo-Neto, F.B. Noronha, L. V. Mattos, F.C. Fonseca, The role of the ceria dopant on Ni/doped-ceria anodic layer cermets for direct ethanol solid oxide fuel cell, Int. J. Hydrogen Energy 46 (2021) 4309–4328, https://doi.org/10.1016/j.ijhydene.2020.10.155.

[40] V.B. Vilela, V.V. Thyssen, F. Fournet Fayard, L. Massim, D.Z. de Florio, A. S. Ferlauto, M.C. Steil, F.C. Fonseca, La0.5Ce0.5O1.75-Catalytic layer for methane conversion into C2 products using solid oxide fuel cell, ECS Trans. 111 (2023) 1957–1964, https://doi.org/10.1149/11106.1957ecst.

[41] M. Coduri, S. Checchia, M. Longhi, D. Ceresoli, M. Scavini, Rare Earth doped ceria: the complex connection between structure and properties, Front. Chem. 6 (2018), https://doi.org/10.3389/fchem.2018.00526.

[42] J. Xu, Y. Zhang, X. Xu, X. Fang, R. Xi, Y. Liu, R. Zheng, X. Wang, Constructing $La_2B_2O_7$ (B = Ti, Zr, Ce) Compounds with Three Typical Crystalline Phases for the Oxidative Coupling of Methane: the Effect of Phase Structures, Superoxide Anions, and Alkalinity on the Reactivity, ACS Catal. 9 (2019) 4030–4045, https://doi.org/10.1021/acscatal.9b00022.

[43] R. Schmitt, A. Nenning, O. Kraynis, R. Korobko, A.I. Frenkel, I. Lubomirsky, S. M. Haile, J.L.M. Rupp, A review of defect structure and chemistry in ceria and its solid solutions, Chem. Soc. Rev. 49 (2020) 554–592, https://doi.org/10.1039/c9cs00588a.

[44] J. Zamudio-García, J.M. Porras-Vázquez, J. Canales-Vázquez, A. Cabeza, E. R. Losilla, D. Marrero-López, Relationship between the structure and transport properties in the Ce1- xLaxO2- x/2 system, Inorg. Chem. 58 (2019) 9368–9377, https://doi.org/10.1021/acs.inorgchem.9b01104.

[45] R. Singh Pal, S. Rana, S. Kumar Sharma, R. Khatun, D. Khurana, T. Suvra Khan, M. Kumar Poddar, R. Sharma, R. Bal, Enhancement of oxygen vacancy sites of La2-xMxCe2O7-δ (M = Ca, Ba, Sr) catalyst for the low temperature oxidative coupling of methane: a combined DFT and experimental study, Chem. Eng. J. 458 (2023), https://doi.org/10.1016/j.cej.2023.141379.

[46] A.M. Arinaga, M.C. Ziegelski, T.J. Marks, Alternative oxidants for the catalytic oxidative coupling of methane, Angew. Chem. 133 (2021) 10596–10609, https://doi.org/10.1002/ange.202012862.

[47] J. Sun, J.W. Thybaut, G.B. Marin, Microkinetics of methane oxidative coupling, Catal. Today 137 (2008) 90–102, https://doi.org/10.1016/j.cattod.2008.02.026.

[48] Z. Zhang, Y. Gong, J. Xu, Y. Zhang, Q. Xiao, R. Xi, X. Xu, X. Fang, X. Wang, Dissecting La2Ce2O7 catalyst to unravel the origin of the surface active sites devoting to its performance for oxidative coupling of methane (OCM), Catal. Today 400–401 (2022) 73–81, https://doi.org/10.1016/j.cattod.2021.11.012.

[49] Y. Zhang, J. Xu, X. Xu, R. Xi, Y. Liu, X. Fang, X. Wang, Tailoring La2Ce2O7 catalysts for low temperature oxidative coupling of methane by optimizing the

preparation methods, Catal. Today 355 (2020) 518–528, https://doi.org/10.1016/j.cattod.2019.06.060.
[50] V. Zymla, F. Honnart, Coke oven carbon deposits growth and their burning off, ISIJ Int. 47 (2007) 1422–1431, https://doi.org/10.2355/isijinternational.47.1422.
[51] M.A. Yatoo, F. Habib, A.H. Malik, M.J. Qazi, S. Ahmad, M.A. Ganayee, Z. Ahmad, Solid-oxide fuel cells: a critical review of materials for cell components, MRS Commun. 13 (2023) 378–384, https://doi.org/10.1557/s43579-023-00371-0.
[52] J. Deboy, R. Hicks, Kinetics of the oxidative coupling of methane over 1 wt% Sr/La2O3, J. Catal. 113 (1988) 517–524, https://doi.org/10.1016/0021-9517(88)90277-1.
[53] Z. Stansch, L. Mleczko, M. Baerns, Comprehensive Kinetics of Oxidative Coupling of Methane over the La $_2$ O $_3$/CaO Catalyst, Ind. Eng. Chem. Res. 36 (1997) 2568–2579, https://doi.org/10.1021/ie960562k.
[54] B. Hu, F. Rosner, H. Breunig, A. Sarycheva, R. Kostecki, M.C. Tucker, Electrochemical conversion of methane to ethylene, olefins, and paraffins using metal-supported solid oxide cells, Int. J. Hydrogen Energy 48 (2023) 33537–33547, https://doi.org/10.1016/j.ijhydene.2023.05.114.
[55] J. Chawla, S. Schardt, P. Lott, S. Angeli, S. Tischer, L. Maier, O. Deutschmann, Detailed kinetic modeling of catalytic oxidative coupling of methane, Chem. Eng. J. 482 (2024) 148719, https://doi.org/10.1016/j.cej.2024.148719.
[56] Y. Peng, Y. Song, I. Razanau, J. Xiao, W. Xiao, D. Hu, G. Wang, Electrochemical conversion of methane to bridge the gap in the artificial carbon cycle, J. Energy Chem. 100 (2025) 286–308, https://doi.org/10.1016/j.jechem.2024.08.050.
[57] D.J. Kuchynka, R.L. Cook, A.F. Sammells, Electrochemical natural gas conversion to more valuable species, J. Electrochem. Soc. 138 (1991) 1284–1299, https://doi.org/10.1149/1.2085774.
[58] S.A. Venâncio, B.J. Moreira Sarruf, G.G. Gomes, P.E. Valadão de Miranda, Multifunctional macroporous solid oxide fuel cell anode with active nanosized ceramic electrocatalyst, Int. J. Hydrogen Energy 45 (2020) 5501–5511, https://doi.org/10.1016/j.ijhydene.2019.06.006.
[59] Z. Gao, J. Zhang, R. Wang, Formation of hydrogen in oxidative coupling of methane over BaCO3 and MgO catalysts, J. Nat. Gas Chem. 17 (2008) 238–241, https://doi.org/10.1016/S1003-9953(08)60057-2.
[60] K. Asami, T. Fujita, K. Kusakabe, Y. Nishiyama, Y. Ohtsuka, Conversion of methane with carbon dioxide into C2 hydrocarbons over metal oxides, Appl. Catal. Gen. 126 (1995) 245–255, https://doi.org/10.1016/0926-860X(95)00042-9.
[61] K. Ramaiyan, A. Benavidez, F. Garzon, Durable electrocatalysts based on barium niobates doped with Ca, Fe, and Y: enhancing catalytic activity and selectivity for oxidative coupling of methane, Chem. Eng. J. 500 (2024) 156976, https://doi.org/10.1016/j.cej.2024.156976.
[62] S. Georges, S.D. Nóbrega, S.K. Cheah, M.C. Steil, Y. Bultel, M. Rieu, J.-P. Viricelle, P. Gelin, Effect of catalyst layer and fuel utilization on the durability of direct methane SOFC, ECS Trans. 69 (2015) 51–59, https://doi.org/10.1149/06916.0051ecst.
[63] Z. Zhan, Y. Lin, M. Pillai, I. Kim, S.A. Barnett, High-rate electrochemical partial oxidation of methane in solid oxide fuel cells, J. Power Sources 161 (2006) 460–465, https://doi.org/10.1016/j.jpowsour.2006.04.139.